Source analysis of acoustic emissions in Aue granite cores under symmetric and asymmetric compressive loads

Arno Zang,1 F. Christian Wagner,1 Sergei Stanchits,2 Georg Dresen,1 Reimer Andresen3 and Mark A. Haidekker4

1 GeoForschungsZentrum, Department 3.2, Telegrafenberg, 14473 Potsdam, Germany
2 Physical-Technical Institute, 26 Polytekhnicheskaya, 194021 St. Petersburg, Russia
3 Behring Municipal Hospital, Department of Radiology, Gimpelsteig 3–5, 14160 Berlin, Germany
4 Center for Medical Diagnostic Systems and Visualization, Universitatsallee 29, 28359 Bremen, Germany

SUMMARY

The effect of stress anisotropy on the brittle failure of granite is investigated under uniaxial compression. Non-standard asymmetric compression tests are performed on cores of Aue granite (diameter 52 mm, length 100 mm), in which 20 per cent of the core top surface remains unloaded. The edge of the asymmetric steel loading plate acts as a stress concentrator, from where a shear rupture is initiated. The propagation of the fracture-related process zone from top to bottom of the core is mapped by microcrack-induced acoustic emissions. Compared to standard uniaxial tests with symmetric loading, in the asymmetric tests both a greater quantity and more localized distributions of emission event hypocentres are observed. The maximum event density doubles for asymmetric (20 events per 10^{-6} m3) compared to symmetric tests. The cluster correlation coefficient, a measure of strain localization in the faulting process, reaches 0.15 for symmetric and 0.30 for asymmetric tests. The clustering of events, however, is found post-failure only. Three different amplitudes are used to determine b-values discussed as a possible failure precursor. Focal amplitudes determined at a 10 mm source distance and maximum amplitudes measured at eight piezoceramic sensors lead to b-values that drop before rock failure. First-pulse amplitudes automatically picked from emission wavelets show no anomaly. First-motion polarity statistics of amplitudes indicate that a shear-crack-type radiation pattern is responsible for 70 per cent of the failure of granite, irrespective of stress boundary conditions. For type-S events with an equal percentage of dilatational and compressional first motions, focal mechanisms are determined by fitting measured first-pulse amplitudes to an assumed double-couple radiation pattern. While hypocentres of large type-S events align parallel to the later fracture plane, their fault plane solutions show no coherent pattern. Spatial views of fracture planes reconstructed from X-ray computed tomograms reveal local small-scale changes in fracture plane orientation. Nodal planes from average fault plane solutions of the microscopic acoustic emission events coincide with the overall orientation of the macroscopic fracture plane azimuth (strike angle) determined from thin sections and tomograms.

Key words: acoustic emission, b-values, cracks, fault-plane solutions, fracture, rock, tomography.

1 INTRODUCTION

Acoustic emission (AE) research on geomaterials in the laboratory commonly pursues two main goals. First, the study of AEs under controlled experimental conditions allows the investigation of the in situ micromechanics of crack growth, crack interaction and failure of rock under stress. Second, brittle rock fracture can be regarded as a process analogous to earthquake rupture since it is found to obey similar statistics for source dimensions over more than eight orders of magnitude, from laboratory subgrain-sized cracks to crustal earthquakes (Hanks 1992). Based on this analogy, AEs can be used

in the failure process to study potential precursor phenomena under controlled conditions in laboratory experiments.

It is found that AE amplitudes increase before failure, which is documented by the drop in the negative slope (b-value) of cumulative amplitude–frequency distributions (Meredith et al. 1990; Main 1992; Sammonds et al. 1992; Lockner & Byerlee 1995; Hori & Maro 1995). In early laboratory studies (Mogi 1962; Scholz 1968) the Gutenberg–Richter frequency–magnitude relationship for earthquake populations was also observed for AE amplitude distributions. Spatial and temporal changes in AE microfracturing patterns (Lockner 1996) and the correlation of AE hypocentre pairs have been used to analyse the localization of deformation during rock failure tests (Hirata et al. 1987; Lockner & Byerlee 1993). State-of-the-art techniques for laboratory mapping of AE hypocentres are summarized in Lockner (1993) and Kusunose (1995). AE focal mechanisms have also been analysed with some success. Two methods can be used, depending on whether AE first-pulse amplitudes or first-pulse signs are evaluated. The first method is called moment tensor inversion (Manthei & Eisenblatter 1993; Shah & Labuz 1995; Ohtsu 1996; Dahm 1996; Grosse et al. 1997); the second method is referred to as polarity study (Satoh et al. 1990; Lei et al. 1992; Meglis et al. 1995).

In this paper potential fracture precursors are evaluated in a comparative study of b-value analysis, hypocentre clustering and focal mechanisms of acoustic emissions during compression tests on granite cores under two different stress boundary conditions. The build-up and release of stress during rock failure is studied in 'standard symmetric' and a new 'asymmetric' uniaxial compression assembly. AE results are compared to observed fracture patterns from X-ray tomograms.

2 EXPERIMENTAL TECHNIQUE

In this section the loading scenarios are discussed and the stress boundary conditions are quantified. A thorough description of the data acquisition system follows, and finally the tomographic fracture inspection technique is described.

2.1 Rock specimens and loading

Uniaxial compression tests were performed on two types of granites from the Erzgebirge, Germany. 'Red' granite (Agr) consists of 30 per cent quartz, 40 per cent plagioclase, 20 per cent K feldspar and 10 per cent mica; the modal composition of 'white' granite (Agw) is 30 per cent quartz, 35 per cent plagioclase, 25 per cent K feldspar and 5 per cent mica. The grain size of Agr ranges from 0.9 to 1.8 mm with an average value of 1.3 mm; Agw grain size ranges from 0.5 to 2.6 mm with an average value of 1.7 mm. Even though Agr is finer grained than Agw, Agr contains larger mica grains. The porosity of Agr is 1.3 per cent, compared to 0.3 per cent for Agw. Cylindrical rock cores 52 mm in diameter and between 110 and 130 mm in length were obtained from quarries at Aue (Agw) and Blauenthal (Agr), located about 40 km southwest of Chemnitz, Sachsen. For convenience, both materials are referred to as Aue granite below. Standard rock cores 100 mm in length were cut from the original drill cores. The ends were polished with 2400 grit (asperity height less than 10 mm). Specimens were dried and kept at room temperature for one month. The cores have a length : diameter ratio of around 2. To calibrate the uniaxial compressive strength we used cores

with ratios between 1.5 and 2.5. To ensure stress homogeneity in the middle of circular cylinders, a ratio of 2.5 is recommended (Paterson 1978). Since stress anisotropy effects are addressed and the stress fields for different boundary conditions inside the cores are quantified (see below), circular cylinders, the lengths of which are about twice the diameters, were chosen.

The experimental set-up consisted of a MTS 4600 kN servo-controlled loading frame (MTS Systems Corporation 1996), a set of eight piezoceramic sensors and a fast storage oscilloscope. The set-up specifications have been described previously (Zang et al. 1996). The effective stiffness of the experimental set-up used in this study including five steel spacers and a 1000 kN force transducer was 1 GN m^{-1}. A standard fixed displacement test with a feed of 0.02 mm per 60 s resulted in sample strain rates of 10^{-5} s^{-1}.

The granite cores were deformed both in standard tests using 'symmetric loading' (Fig. 1a) and in tests with 'asymmetric loading', in which 20 per cent of the core top surface remained deliberately unloaded (Fig. 1b). As far as we know, in previous literature no compression tests with 'asymmetric loading' have been reported. The stress boundary conditions in the two loading scenarios were very different. To illustrate this, stress contours were calculated with a finite element rock model (Appendix A). In Fig. 1 minimum principal stresses calculated for symmetric loading ($-126 < S_3 < -94$ MPa) and asymmetric loading ($-562 < S_3 < 9$ MPa) are normalized to the extreme values (-126 MPa in the symmetric case and -562 MPa in the asymmetric case); tension is positive. The contour line 0.75 defines the rock volume in which the minimum principal stress exceeds 75 per cent of the corresponding extreme value. In the asymmetric case high stress concentrations occur at the core surface where loaded and unloaded parts are adjacent (Fig. 1b). From tensile and shear stress distributions (Appendix A) it follows that the specimen fails by shear rupture (with a tensile component) that propagates from top to bottom (Fig. 1b, dashed line). For comparison, stress contours of a standard
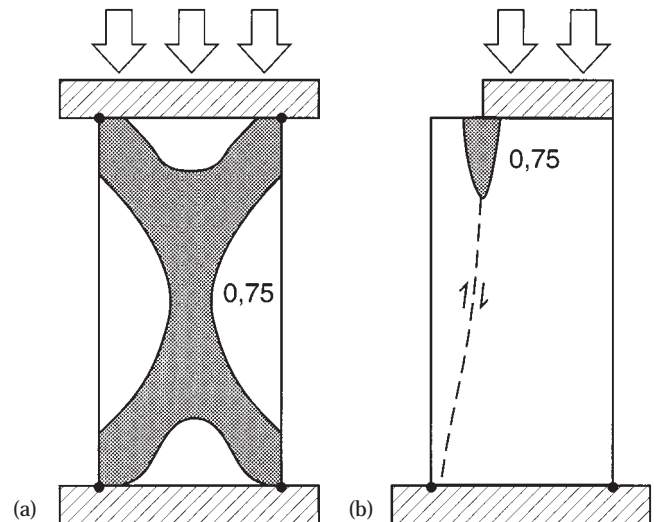

Figure 1. Contour plot of stress concentration factor 0.75 (shaded area) during (a) symmetric and (b) asymmetric compressive loading. Line 0.75 defines the rock volume in which the minimum principal stress exceeds 75 per cent of the corresponding extreme value [$S_3 = -126$ MPa in (a) and $S_3 = -562$ MPa in (b)]. Hatched areas indicate compression plates. Dashed line in (b) indicates expected shear rupture path.

symmetric test are given, showing the well-known cone-shaped stress contours (Fig. 1a), which are caused by material contrasts (rock/steel) and end-cap friction (Peng & Johnson 1972; Paterson 1978).

2.2 Acoustic emission measurements

Eight piezoceramic sensors were used in each displacement-controlled test to determine the AE hypocentres for both loading scenarios (Fig. 2, 1–8). Piezoelectric transducers were attached with springs to the sample. The spring brackets were placed in planes located 30 mm from the top and bottom of the cylinder. The piezoceramic crystals were encapsulated in brass housings that conformed to the cylindrical surface of the sample. The housings were bonded to the sample with machine
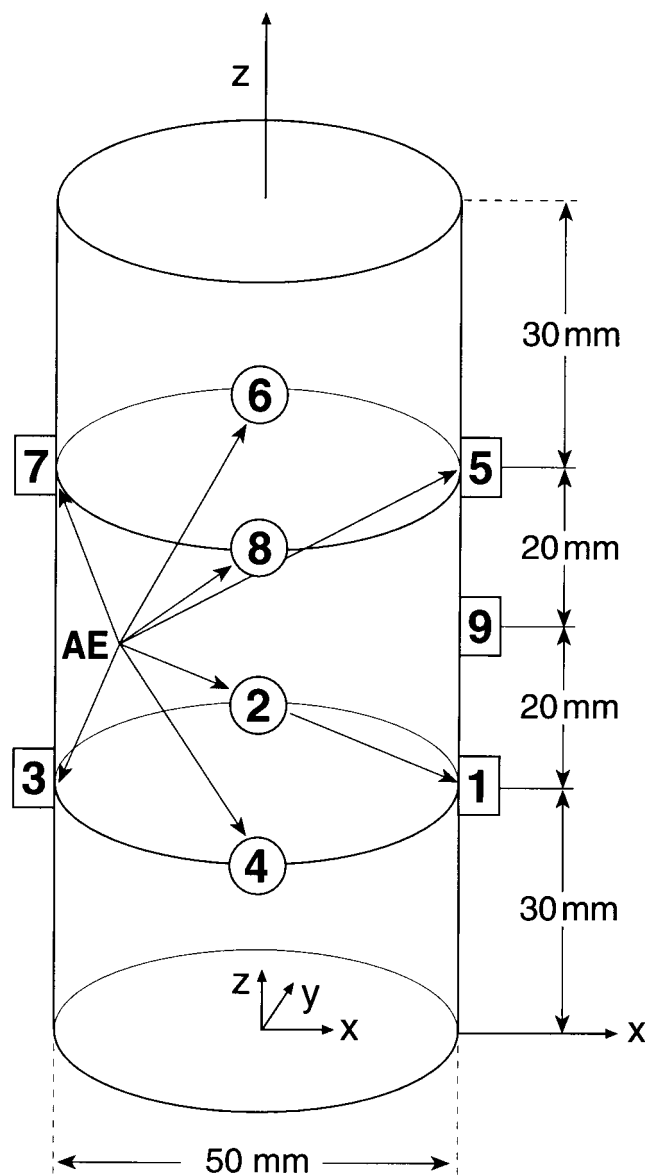
Figure 2. Set-up of eight piezoceramic sensors (1–8) for the determination of acoustic emission hypocentres in deformed rock cores and one broad-band sensor (9) for continuous registration of wavelet parameters. Origin of the coordinate system is at the centre of the cylinder's bottom surface.

grease. The set-up contained one broad-band sensor (Fig. 2, 9) with a calibrated transfer function stable within 5 dB in the frequency range 200 kHz–1 MHz.

A transient memory (PSO 9070, Krenz GmbH) with 12 channels, 10-bit vertical resolution and a sampling frequency of 20 MHz was used to store AE wavelets. Using a sampling frequency of 5 MHz (time resolution 0.2 μs) and a wavelet length of 512 byte, 999 AE waveforms were stored with a maximum rate of 100 AE s^{-1}. Subsequently, the transient memory was transferred to the hard disk of a PC. The transfer time for 999 AEs was about 40 s. A hard disk partition of 200 Mbyte allowed the storage of about 22000 AE wavelets using eight channels. The trigger level for all channels (except the broad-band sensor) was set to a constant 5 mV for standard experiments and increased to 10 or 15 mV in some tests to limit the number of AEs detected.

Signals detected with the broad-band sensor were pre-amplified by 40 dB and analysed online with the PC card SEK 3243 (Fraunhofer-Institut, Dresden) on a separate computer. Eight wavelet parameters were determined (event number, time of first threshold crossing, duration time of signal, time between two signals, ring-down counts, rise time to the maximum amplitude, maximum amplitude and pulse energy). The displacement, force and time-base of the experiment were recorded with the MTS TestStar software using a third PC. All three PCs were synchronized by a starter pulse.

Hypocentre determination from measured AE wavelet data is carried out using three different iteration algorithms [the Gaussian (Lockner et al. 1992), modified Gaussian (Zang et al. 1996) and Downhill Simplex (Press et al. 1987) methods]. For the present study we concentrate on results obtained with the Simplex method. The comparison of event densities and hypocentre distributions is then possible on a quantitative basis. The precision of the source location was 3 mm for both sandstone (Zang et al. 1996) and granite specimens. This value was derived from active tests on several cores using one of eight sensors as a seismic source with a 400 V input signal. Reducing the input voltage with a sliding resistor (1 MV to 1 kV), the maximum location error increased to 15 mm for small-amplitude events. Low-amplitude pulses are expected in the post-failure regime of rock fracture experiments. In this regime the iteration algorithm was improved by rejecting channels with low amplitudes one by one (worst channel rejection). Second, in order to minimize hypocentre errors in different regions within the specimen, besides hypocentre coordinates, traveltime residuals are also considered. For standard hypocentre calculations the cut-off value of the residual was set at 5 μs; for highest-quality events, for example fault plane solutions, the value was 1 μs.

2.3 Fracture inspection by X-ray computed tomography

Before and after deformation, selected cores were analysed by high-resolution (0.2 mm) computer-assisted tomography (CT) with a Siemens Somatom DRH device (Andresen et al. 1997). The deformed rock core was scanned in three orthogonal planes with a 2 mm slice thickness and 2 mm distance between rock slices. From 50 horizontal slices (Fig. 2, x–y projections) and 50 vertical slices (Fig. 2, 25 x–z and 25 y–z projections) a spatial view of the fracture plane was reconstructed using two features of visualization packages (volume rendering and trace algorithm). Subtracting the rock matrix, which is assumed to

be the same before and after loading, the fracture planes of deformed cores can be viewed from arbitrary angles.

3 EXPERIMENTAL RESULTS

Results from 20 symmetric compression tests are used to determine the mechanical parameters (e.g. uniaxial compressive strength, Young's modulus, deformation energy) of white and red Aue granite. 10 asymmetric tests are performed with different AE trigger levels to capture the fracture propagation with no or limited loss of AE wavelets in the transient memory. From these, two symmetric (Ag5r, Ag11w) and two asymmetric tests (Ag1r, Ag5w), with maximum exploitation of AEs during the rupture process, are chosen, each performed on both red and white granite samples. The findings reported below are 'typical' of the failure in Aue granite. They are confirmed by a suite of experiments operated with 12 sensors, where one sensor was used as a feedback signal to the loading system. AE rate-controlled experiments are discussed in a separate paper.

3.1 Hypocentre distribution and fracture growth

In Table 1 the first two blocks of data list located AE event numbers obtained from modified Gaussian and Simplex iteration algorithms. From 999 events detected per file (rows a–f) the numbers in Table 1 indicate the located events

depending on loading interval (Fig. 3, a–f) and iteration method used. The first block summarizes results from the modified Gaussian algorithm, the first column listing the total number of located events and the second column the high-quality hypocentral data with traveltime residuals smaller than 5 ms. The second block contains located event numbers from the Simplex method. The two different column headings refer to different versions of the localization algorithm (trig ch = all triggered channels used; ch > 6 = worst channel rejection method). Data in the third block of Table 1 are calculated from Simplex hypocentre distributions only, to be comparable on a quantitative basis.

The diagrams in Fig. 3 show the cumulative detected (not located) number of AE events and stress (for symmetric tests) or force (for asymmetric tests) versus time of loading for the four granite samples from Table 1. Since the top and bottom load surface areas are different in asymmetric tests (Fig. 1b), the resulting stress pattern inside the cylinder is complex (Fig. A1). Therefore, force data are shown in Figs 3(c) and (d). During 'symmetric failure' the cumulative event number increases dramatically (Fig. 3a: t = 1800 s; Fig. 3b: t = 1980s). In 'asymmetric failure' a first sharp increase in event number occurs much earlier than in the symmetric tests. This early event accumulation is due to the initiation and growth of a fracture, starting in the high stress concentration at the top end of the specimen (Fig. 1b). About 1000 AEs are emitted

Table 1. Comparison of acoustic emission results of two symmetric (Ag5r, Ag11w) and two asymmetric tests (Ag1r, Ag5w) on Aue granite. The number of located AE versus stress regimes is summarized using the modified Gaussian method (first block) and the Simplex method (second block). Block three lists the maximum value of current cluster analysis C(r = 10), the fractal dimension D of hypocentre distributions, the maximum event density value and microfracturing event types obtained from the radiation pattern analysis according to their occurrence. The last row indicates the AE trigger level. To be comparable on a quantitative basis, in block three only Simplex hypocentre data are used.

Loading Core	Symmetric				Asymmetric			
	Ag5r		Ag11w		Ag1r		Ag5w	
Modified Gaussian	all R	R < 5 ms	all R	R < 5 ms	all R	R < 5 ms	all R	R < 5 ms
a	662	49	698	182	607	257	735	280
b	647	23	–	–	630	181	722	333
c	370	14	–	–	640	67	591	11
d	301	4	–	–	664	8	403	8
e	24	0	–	–	–	–	337	37
f	–	–	–	–	–	–	239	8
Downhill Simplex	trig ch	ch > 6	trig ch	ch > 6	trig ch	ch > 6	trig ch	ch > 6
a	121	441	161	593	555	727	446	812
b	63	294	1	42	310	614	65	625
c	8	143	–	–	123	296	6	387
d	0	28	–	–	11	66	1	45
e	0	23	–	–	–	–	1	20
f	–	–	–	–	–	–	1	13
C(r = 10)	0.13		0.15		0.20		0.30	
D	1.9–2.8		1.7–2.4		1.2–2.5		1.3–2.1	
AE/ccm	10		12		25		20	
radiation S	70		63		81		70	
pattern T	18		19		08		20	
type (%) C	12		18		11		10	
Trigger (mV)	5		15		10		15	

Agr = red Aue granite; Agw = white Aue granite; R = traveltime residual; ch = channel; C(r = 10 mm) from current cluster analysis (Zang et al. 1996); D = fractal dimension from classical C(r) solution (Hirata et al. 1987); AE/ccm = calibrated maximum event density (events per 10^{-6} m3); type-S = shear, type-T = tensile, type-C = implosion/collapse source of AE; a–f: stress intervals from Fig. 3.
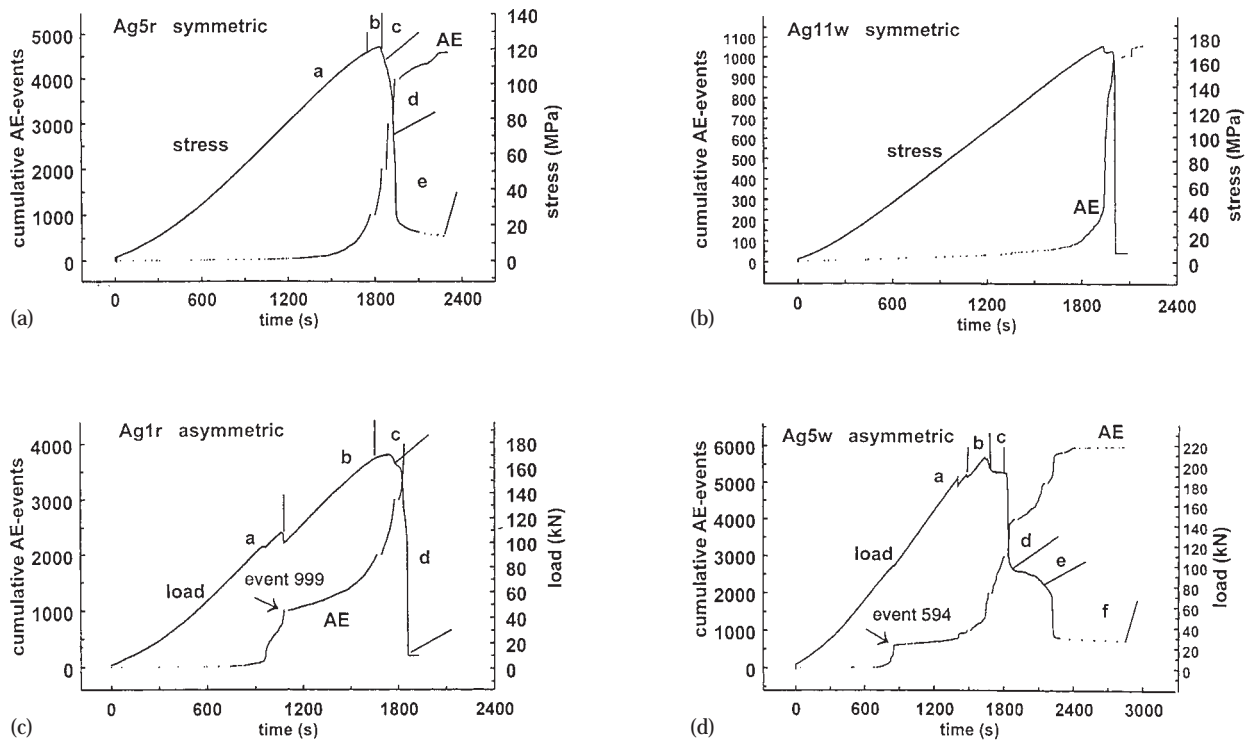
Figure 3. Cumulative number of detected events and stress for symmetric or force for asymmetric loaded cores as a function of time for Aue granite specimens Ag5r (a), Ag11w (b), Ag1r (c) and Ag5w (d).

in conjunction with the asymmetric fracture of Ag1r (Fig. 3c: event 999, $t = 1020$ s) and about 600 AEs accompany the fracture of Ag5w (Fig. 3d: event 594, $t = 850$ s). Similar to symmetric tests the maximum number of AE events occurs during final failure of the specimen (Fig. 3c: $t = 1800$ s; Fig. 3d: $t = 1860$ s). The striking difference between the loading scenarios is the occurrence of a localized shear fracture in 'asymmetric tests' as compared to the distributed cone fracturing in 'standard uniaxial symmetric' compression tests. In the following, differences in AE characteristics during 'asymmetric fracture' (Ag1r, Ag5w) and 'symmetric fracture' propagation (Ag5r, Ag11w) are analysed.

According to Table 1, the trigger level during the deformation of core Ag1r (10 mV) is lower than during the deformation of Ag5w (15 mV). Using a standard trigger level of 5 mV and averaging over 30 experiments, the number of AEs detected is increased by applying an asymmetric instead of a symmetric load and by using white instead of red granite. On average the ratio of events detected from asymmetric compared to symmetric tests is 1.9 for Agr and 5.6 for Agw. The ratio of detected events during symmetric deformation of Agw compared to Agr is 1.9. Time gaps (40 s duration) in intervals of the 999 AE events of the cumulative event curve in Fig. 3 are due to the dead time of the transient recorder. Time gaps in between indicate real (low) event activity in the corresponding time section.

In Fig. 4 three orthogonal projections (x–y, x–z, y–z) of AE hypocentre density distributions are shown versus loading interval for a symmetric test (Ag5r). Letters a–e refer to the loading intervals indicated in Fig. 3(a). The maximum event density (black) in the contour plot is 40×10^6 AE m^{-3} ($= 40$ AE cm^{-3}); white denotes zero event activity. For stresses below the uniaxial compressive strength of the core (Fig. 3a,

129 MPa; loading intervals a–b) events cluster in the central (Fig. 4, x–y projection) and lower parts (Fig. 4, vertical projections) of the core. The evolution of event clusters, in general, agrees with the anticipated stress concentration in the core (Fig. 1a), whereby the lower cone fracture event activity dominates. In the post-failure regime (Figs 3a and 4, intervals c–e), event density spreads towards the mantle of the cylinder (Fig. 4, horizontal slice); at this time the final throughgoing cone fracture is formed. Later in the post-failure process (Figs 3a and 4, regimes d–e) the maximum event density drops below 4×10^6 AE m^{-3} and shows a more homogeneous distribution. Note that absolute event density values depend on the total number of located events incorporated (Fig. 4, Ev). To be comparable on a quantitative basis, event density values shown in Table 1 (also in Figs 7 and 8) are based on a constant number of events (80) and on a standardized hypocentre algorithm (Simplex method). In the following this value is called calibrated event density. In Fig. 4 modified Gaussian hypocentre data are seen to map the shift in event density from pre-peak to post-peak stress intervals based on a greater number of events (Table 1, Ag5r). The cone fracture pattern form core inspection was too complex to incorporate into Fig. 4. Two sets of subparallel fractures are formed in the region of isostress contours from Fig. 1(a). The absence of AE at the loaded ends of the cylindrical specimen is presumably due to end-cap friction. Both red and white granite samples show very similar mechanical responses upon symmetric loading, even though the average uniaxial compression fracture strength of the red granite is 134 ± 7 MPa compared to 173 ± 26 MPa for the white granite. The smaller number of events in test Ag11w is due to the higher trigger level (Table 1, 15 mV).

The hypocentre density distribution for asymmetric loading
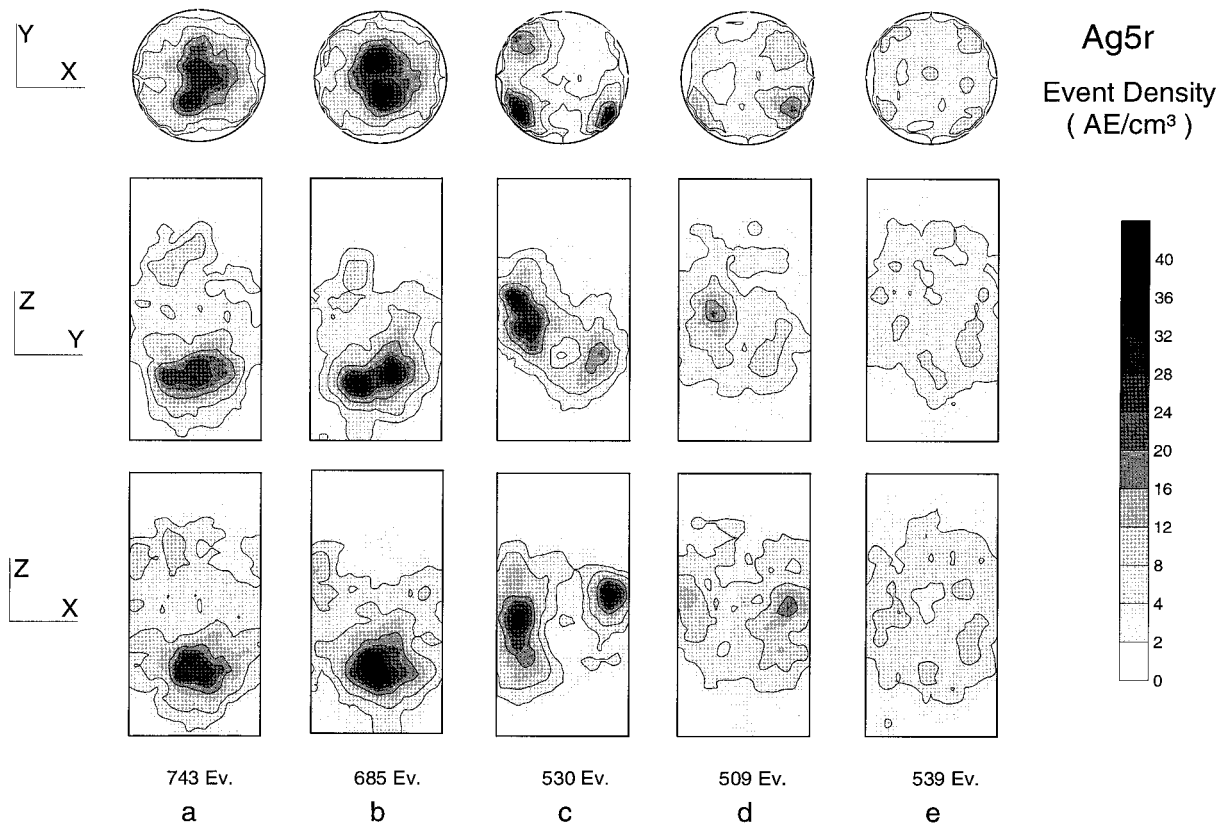
Figure 4. Emission hypocentres determined from the modified Gaussian method plotted as density contour intervals in a symmetric compression test on core Ag5r for stress regimes a to e as defined in Fig. 3(a).

sample Ag5w is shown in Fig. 5. For reference the failure plane from X-ray tomograms and microscopic inspection of the deformed core is shown in three orthogonal projections in Fig. 5, a1. Only data from loading interval a of Fig. 3(d) related to the formation of the shear fracture are plotted. In contrast to the symmetric test (Fig. 3a), in the asymmetric test no AE data are lost during fracture nucleation and propagation due to the dead time of the transient recorder (Fig. 3c). Maximum density (black) in the contour plot represents 20×10^6 AE m^{-3}. To illustrate the growth of the fracture, the first 999 AEs are divided into five intervals with events located by the Simplex method. From the rise of cumulative AEs (Fig. 3d, t = 860 s), the fracture propagation is assumed to be completed at event number 594. Fig. 5 maps four stages of fracture growth (a1, a2, a3 and a4) and one stage of stress accumulation in the remaining part of the rock cylinder (a5). The corresponding time intervals are as follows: a1 492–819 s; a2 819–833 s; a3 833–850 s; a4 850–857 s; a5 858–1484 s. The x–z projection of the event density contours traces the shear fracture from top to bottom of the core (Fig. 5 a1–a4, x–z). The y–z projection represents a view onto the fracture plane, which is growing from top left (Fig. 5 a1, y–z) to about 10 mm above the bottom surface (Fig. 5 a4, y–z). The x–y projection (core top view) shows that the contour lines of high event density coincide with maximum shear stress from finite element calculations (Fig. A1b). In the vertical projections (x–z, y–z) the maximum event density occurs 25 mm below the core top surface. After the formation of the shear fracture is completed the emission activity is shifted into the remaining part of the cylinder (Fig. 5, a5).

3.2 Clustering of events (C- and D-values)

The correlation integral (C(r), Hirata et al. 1987) is a quantitative measure that documents changes in spatial distributions of AE hypocentres during rock failure. Using a constant separation distance r for the hypocentre pairs C(r = const.), the time variation of the correlation coefficient can be investigated when rock failure is approached (Zang et al. 1996). Analogous to C(r)-values, C(r = const.)-values document localized (high C) and delocalized (low C) microfracturing events. In Fig. 6, C(r = const.)-values are calculated for a moving cluster of 50 AEs with fixed radius (r = 10 mm). This current cluster analysis is carried out for a symmetric (Fig. 6a) and an asymmetric test (Fig. 6b). A significant increase of the correlation coefficient occurs during the symmetric test [Fig. 6a: C(r = 10 mm) = 0.13 at t = 1800 s] corresponding to the building of the main cone fracture of specimen Ag5r. During asymmetric testing the first two elevated correlation coefficients are connected with the formation of the shear fracture (Fig. 6b: t = 960, 1080 s) and the third to the formation of the final fracture of sample Ag1r (Fig. 6b: t = 1700 s).

Under the assumption of self-similar hypocentre distributions, C(r) is proportional to r^D, where D is the correlation coefficient (Grassberger 1983) or the fractal dimension (Lei et al. 1992). For a homogeneous distribution of hypocentres, D = 3. A decrease in D indicates a change in the spatial hypocentre distribution from volume filling to a planar structure, i.e. the fault plane (Lockner & Byerlee 1995). The D-value can be estimated from the slope of a log–log plot of C(r) versus r. Note that this analysis is different and more time
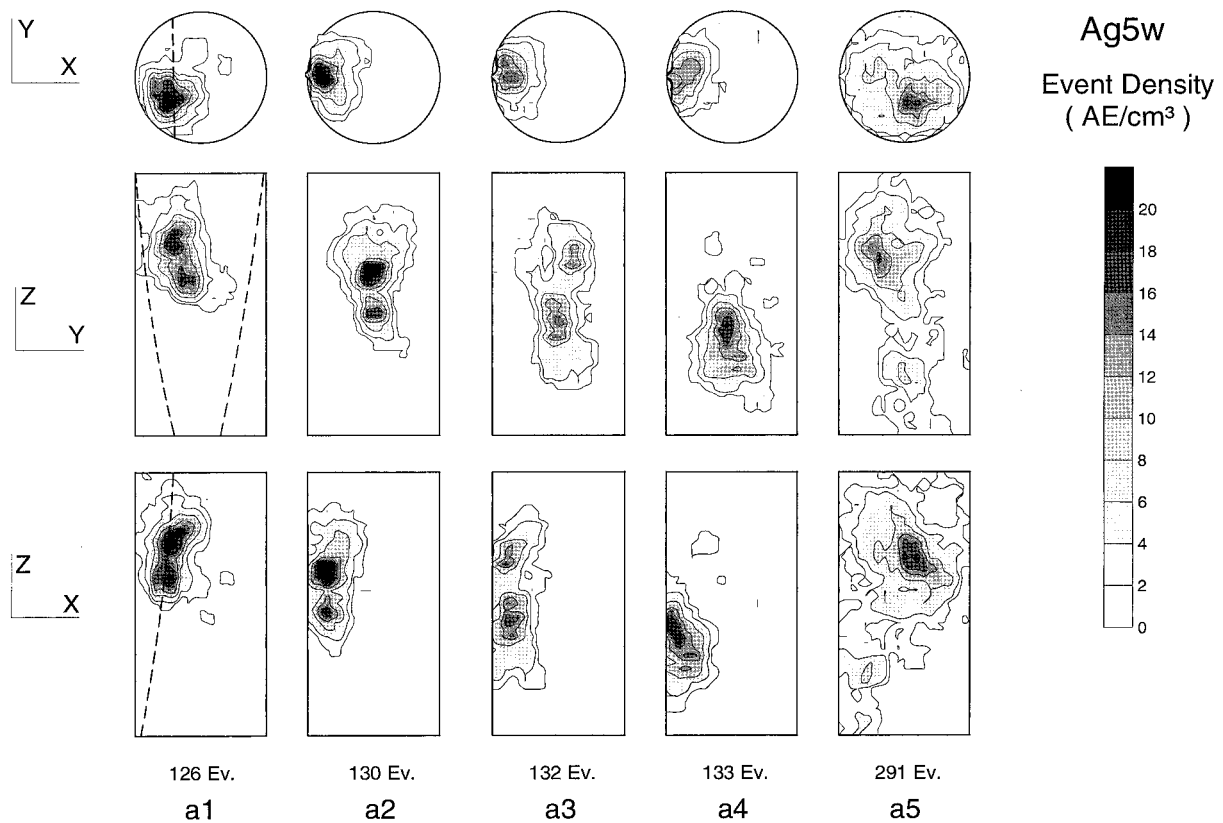
Figure 5. Event density contours determined from Simplex hypocentre data in stress regime a of Fig. 3(d). To map asymmetric pre-fracture growth, events from regime a are subdivided into four stages of pre-fracture propagation (a1 to a4) and one stage of stress accumulation after the pre-fracture has formed (a5). The pre-fracture plane from core inspection is indicated as a dashed line in a1.

consuming than that described in Fig. 6. In Table 1 minimum and maximum D-values for each experiment are listed.

In Figs 7 and 8, the temporal variation of D is plotted for an asymmetric (Fig. 7a) and a symmetric test (Fig. 8a). D-values are obtained from least-squares fits. The error bar indicates the deviation of the slope of a log–log plot of C(r) versus r at the end-member points of a moving window of 80 points with respect to the slope determined in the centre of the window. The middle plot in each figure shows the calibrated maximum event density value, while the bottom plot shows the corresponding load-time history with the cumulative number of events. Calibrated density values are determined from a moving window of 80 AEs with a shift of 20 AEs. In the asymmetric test the D-value drops to 1.2 at $t = 1075$ s (Fig. 7a), while the event density rises to 25×10^6 AE m^{-3} (Fig. 7b). D recovers after the fracture growth is completed (Fig. 7c, force drop at $t > 1075$ s). The same behaviour is observed for core Ag5w, where the minimum drop of D was 1.3 (Table 1). The drop in D is less pronounced in symmetric tests (Fig. 8, Table 1). The calibrated maximum event density in symmetric tests (Fig. 8b) is only one-half of the AE density reached in asymmetric tests (Fig. 7b). None of the hypocentre-distribution-related AE parameters investigated indicated a significant precursor anomaly in Aue granite either in asymmetric (Fig. 7, $t < 1060$ s) or in symmetric tests (Fig. 8, $t < 1930$ s).

3.3   Amplitude and energy statistics (b-value)

In this section the maximum amplitude from the source location sensors and the acoustic energy from the broad-band sensor are evaluated statistically. From the maximum amplitude of each channel an average focal amplitude is calculated:

$$\bar{A}_0 = \sqrt{\frac{1}{k} \sum_{i=1}^{k} \left(\frac{r_i}{10} A^i_{max} \right)^2}; \qquad r_i \ [\text{mm}] \qquad (1)$$
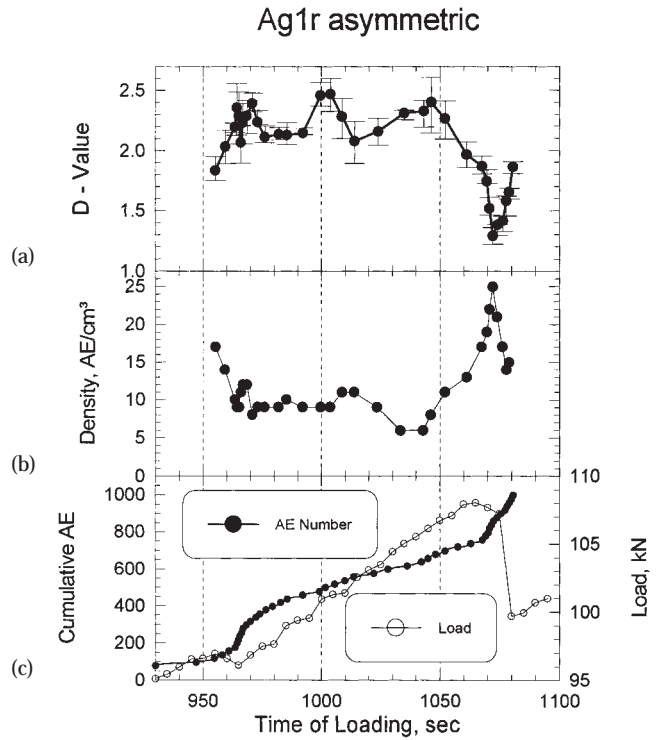
where k is the number of channels used for hypocentre determination and r_i is the hypocentre distance to the ith receiver transducer. It is important to emphasize that the r2 correction in (1) is for geometric spreading of waves. No account is taken of anelastic absorption. The latter assumption could be justified by high Q of the granite samples, and an estimate of the number of cycles could be made from source to receiver given the velocities and frequencies used. This is a major improvement on previous work (e.g. Main et al. 1993), where locations were not attempted. The average focal amplitude $\bar{A}_0$ in (1) is calculated on a reference sphere (radius 10 mm), with its origin at the AE position assuming spherical spreading. The focal amplitudes for the first 999 AEs detected during the asymmetric deformation of Ag5w are plotted versus time in Fig. 9(a). The fracture event at $t = 850$ s causes an increase in focal amplitude. For comparison, Fig. 9(b) shows the energy equivalent of events (Zang et al. 1996) detected with the broad-band sensor for the same time interval. The acoustic emission energy (Fig. 9b, squares) increases at 850 s. Additionally, several increases of AE energy are observed later in the experiment that correspond to mechanical responses of the specimen (Fig. 9b, force = triangles). Note that energy equivalents (Fig. 9b) are registered continuously, in contrast
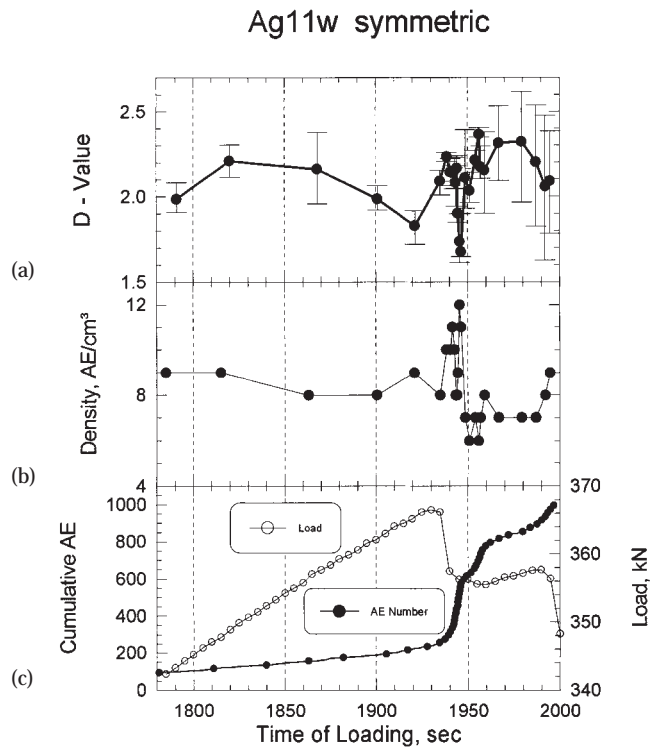
© 1998 RAS, GJI **135**, 1113–1130
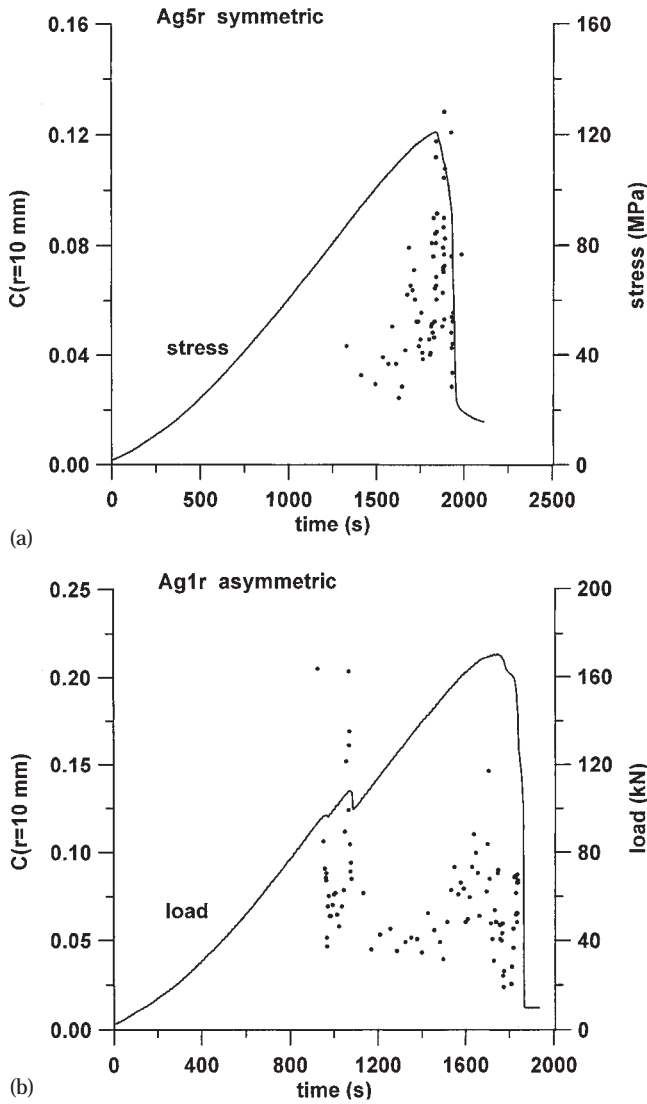
Figure 6. Current cluster analysis C(r = 10 mm) of a moving window with 50 AEs determined by the Simplex algorithm versus time for (a) a symmetric and (b) an asymmetric test.

Figure 7. (a) Fractal dimension D of event hypocentre distribution obtained from correlation integral analysis, (b) maximum event density and (c) loading curve with accumulated event number versus time of the asymmetric test on core Ag1r. Stress drop of the 'asymmetric failure' occurs at 1075 s.

to amplitude values (Fig. 9a), which are limited by the dead time of the transient recorder.

From averaged first, averaged maximum and averaged focal amplitudes of location sensors, cumulative amplitude–frequency distributions are calculated according to the Gutenberg–Richter relationship. The negative slope of cumulative amplitude–frequency distributions, the so-called b-value, is calculated from a window of 80 AEs, which is shifted by 20 AE increments, using a least-squares fit. The b-value is shown versus time for the asymmetric test on core Ag1r (Fig. 10) and for the symmetric test on core Ag5r (Fig. 11). In Fig. 10(a) the b-values calculated from maximum and focal amplitudes show a significant (e.g. 42 per cent for A_{max}) drop before the shear fracture at time t = 1075 s. A similar drop in b-value calculated from
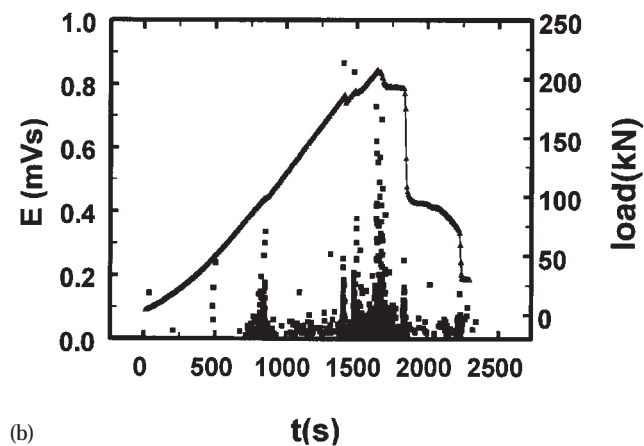
Figure 8. (a) Fractal dimension of hypocentre distribution, (b) maximum event density value and (c) loading curve with accumulated event number versus time of the symmetric test on core Ag11w. Stress drop of the 'symmetric failure' occurs at about 1930 s.
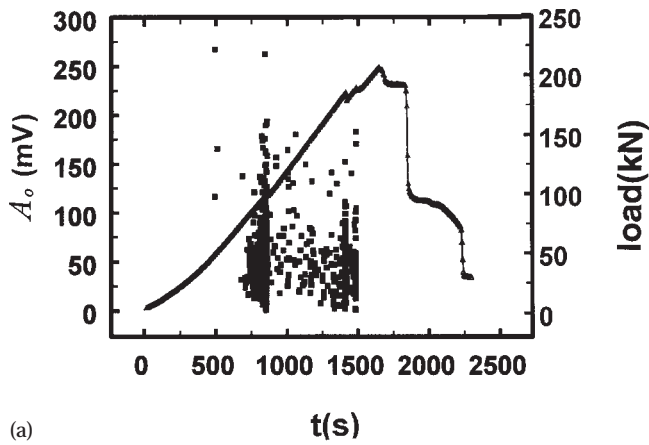
(a)

(b)

Figure 9. (a) Average focal amplitude and (b) pulse energy equivalent versus time of loading in the asymmetric compression test on core Ag5w. Focal amplitudes in (a) are calculated from eight location sensors for the first 999 events of the transient memory. Energy pulses in (b) are determined from continuous registration of the broad-band sensor leading to 2652 AEs.

first-pulse amplitudes is not observed. The reason for this may be an artefact of the automatic first-motion picker, which is related to the noise level. A physical explanation would require a mechanism producing first-pulse amplitudes that are independent of the following AE wavelet, no matter how big the event is. Since this problem is not yet solved, first-pulse amplitude statistics are not considered in the following diagrams (i.e. Fig. 11). The drop in b-value of the symmetric test on core Ag5r (Fig. 11a) is comparable (e.g. 36 per cent for A_{max}) to that of the asymmetric test on core Ag1r, even though the time spans are different. The time gap in b-values of Fig. 11 is due to the storage of the transient memory on the hard disk (see also the comment on Fig. 9). For reference, event activity and force data are plotted in Figs 10(b) and 11(b).

In contrast to hypocentre correlation data (Figs 6, 7 and 8), b-values from emission amplitudes indicate a precursor anomaly; that is, they show a drop before a mechanical response of the core is observed (Figs 10 and 11). The b-values calculated from energy frequency distributions detected with the broad-band sensor give similar results.
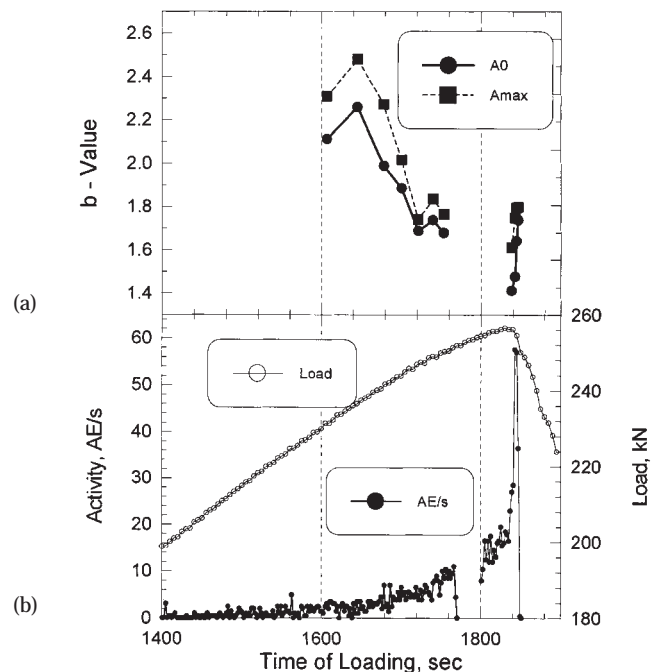
Ag1r asymmetric
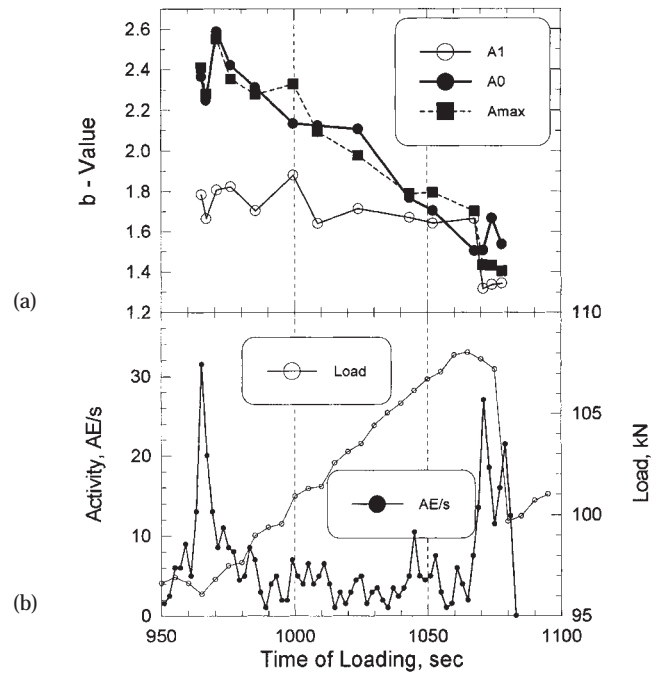
(a)

(b)

Figure 10. (a) The b-value calculated from the first pulse (A_1), the maximum (A_{max}) and the focal amplitude (A_0) of acoustic emission event wavelets of the asymmetric test on core Ag1r. (b) The event rate and force versus time data are shown for reference.

Ag5r symmetric

(a)

(b)

Figure 11. (a) The b-value calculated from the maximum (A_{max}) and the focal amplitude (A_0) of AE wavelets of the symmetric test on core Ag5r. (b) For reference the event rate and force versus time data are shown. Dead time of event recording is from 1770 to 1800 s.

3.4 Focal mechanisms

For located AE events, first-pulse arrival times (t_1) and first-pulse amplitudes (A_1) are picked automatically. The polarity value pol of a single event is calculated by

$$pol := \frac{1}{k} \sum_{i=1}^{k} sign(A_i^1), \tag{2}$$

where i and k are defined analogous to (1). The polarity is used to separate type-S events ($-0.25 \le pol \le 0.25$) from type-T ($-1 \le pol < -0.25$) and type-C sources ($0.25 \le pol < 1$). Our simplistic approach to distinguish between fracture types is to calculate the ratio between piezograms with positive and negative first motions. If most sensors have compressional or dilatational first motions, the events are named type-T and type-C, respectively. Otherwise (polarities between -0.25 and 0.25), they are named type-S. Signal polarity is calibrated with pencil lead break and steel ball drop experiments. The procedure is tested with a resin specimen with a single defect. From both ends of a penny-shaped crack, located in the centre of a cylindrical resin specimen and tilted $45°$ to the vertical compression direction, wing (tensile) cracks are forced to initiate. Only dilatational (positive) pulses with large first motions are detected on the eight-sensor array from Fig. 2. For type-S microfractures, having equal portions of compressional (negative) and dilatational pulses, nodal planes are determined on a lower-hemisphere equal-area plot. From all events emitted before and during the fracture of specimen Ag5w (Fig. 3d, AE numbers $N \le 594$), 70 per cent show type-S polarity, 20 per cent type-T and 10 per cent type-C (Table 1). From Table 1 it is clear that type-S sources dominate failure in both symmetric and asymmetric granite compression tests. All findings from Table 1 are confirmed by uniaxial compression tests with 12 instead of eight detection sensors.

In Fig. 12, single fault plane solutions of the six largest ($143 < A_0 < 175$ mV) type-S events are seen in x–z view. For reference the polarities of eight sensors are shown on six side focal spheres on the right. In contrast to the standard lower-hemisphere projections used in seismology (x–y view), the side focal sphere projection used in Fig. 12 (x–z view) involves cutting the focal sphere in the x–z plane and projecting polarity data onto a Schmidt equal-area net towards the positive y-direction. Since asymmetric tests require fracture mapping in the x–z plane, we work with (unconventional) side focal sphere projections. Fault plane solutions are obtained from first-motion arrival data of acoustic emission wavelets. Measured first-pulse amplitudes of eight wave trains are fitted to the theoretical radiation pattern of a pure double-couple
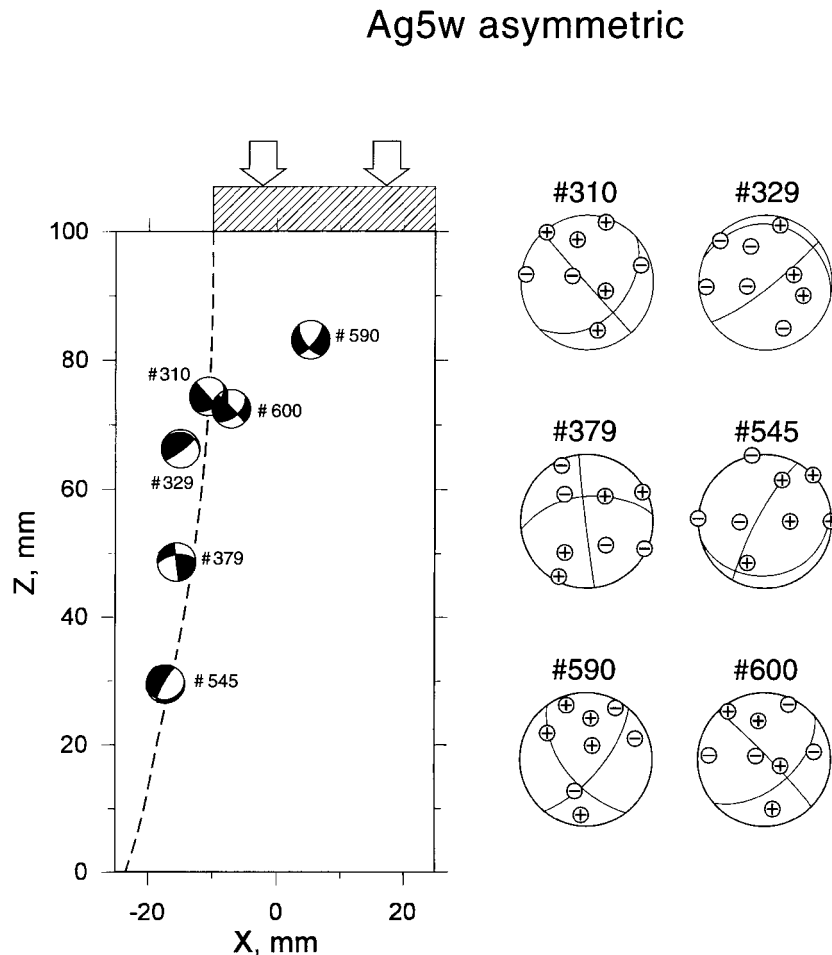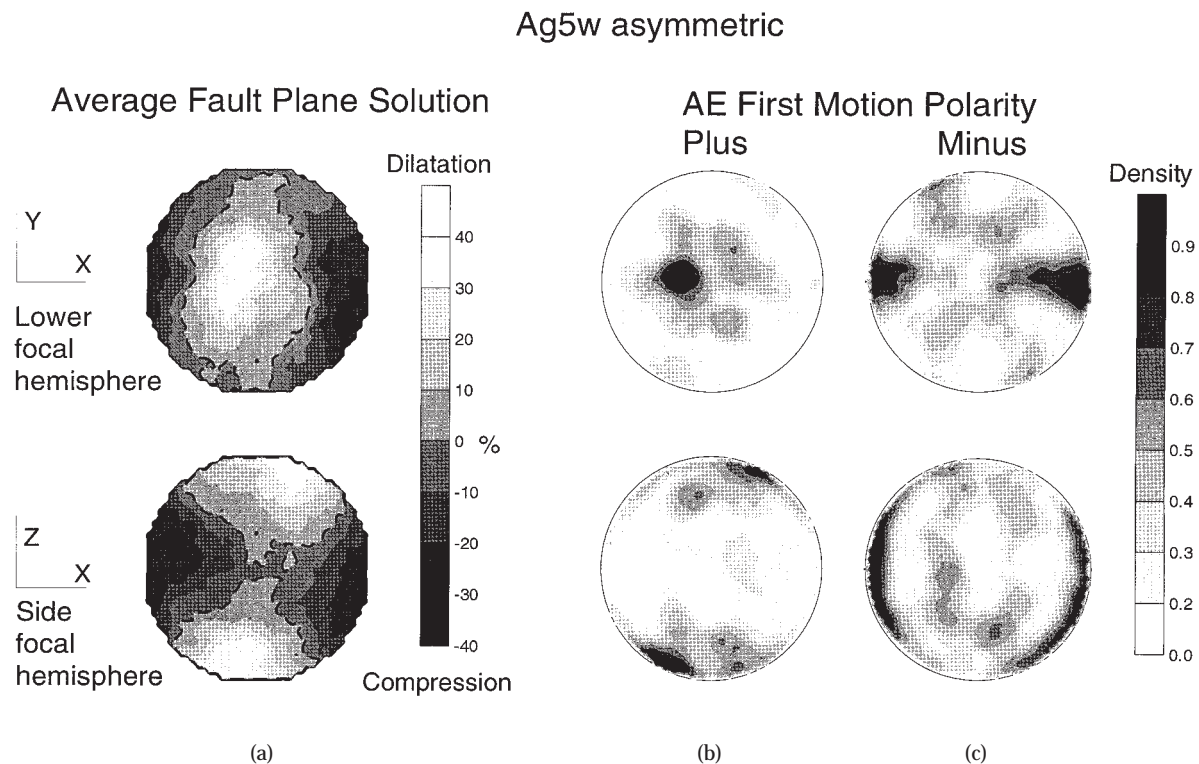

Ag5w asymmetric

Figure 12. Fault plane solutions of the six largest (in terms of average focal amplitude) type-S microfracturing events during the asymmetric test on core Ag5w. Only events before and during fracture are considered. Dashed line indicates trace of fracture plane. The polarities of eight sensors are shown on focal spheres on the right. Side focal hemisphere projections (x–z) are used, where black (left) and plus signs (right) indicate compression.

source assumed at the respective location of the acoustic event. Again, the Simplex method is used to determine the magnitude and orientation (three angles) of the double-couple source. Polarities at odds with the proposed solution (Fig. 12, right) may indicate deviations from a pure double couple. Note that the sign convention of the focal spheres (Fig. 12, right) is reversed from that commonly used in seismology due to the calibration of our piezoceramic sensors (minus equals compression). The black on the focal spheres (Fig. 12, left) indicates compression. From Fig. 12 it is evident first that large type-S events align along the future shear plane in the rock (Fig. 12, dashed line), and second that nodal plane orientations of large-amplitude events show no coherent pattern, as expected for the asymmetrically induced shear rupture plane. Note that, assuming the radiation pattern of pure double couples, the reliability of single fault plane solutions for type-S events depends on the number of channels and the quality of first arrivals.

For selected cores, average fault plane solutions of single fault plane solutions are calculated. For this purpose, each single fault plane solution represented in a conventional lower-hemisphere projection (x–y) or unconventional side focal sphere projection [x–z (e.g. Fig. 12), y–z] is divided into 20 × 20 possible accumulation cells. In each cell the signs of first-pulse motions are added for all events located. Recall that first-pulse amplitudes are needed to determine single fault plane solutions, from which only first-pulse polarities are used in the accumulation process. Summarized polarity cell data are normalized to the number of events located. The method used here is more similar to that of composite fault plane

solutions (e.g. Angelier 1984, the method of P and T dihedra) than to methods where moment tensors are summed to give the overall strain field (Jackson & McKenzie 1988). In Fig. 13(a) the average fault plane solution of 212 located type-S events (including small- and large-amplitude events) is plotted in lower- and side focal hemisphere projection. The greyscale indicates percentage values of dilatational (white) and compressional pulses (black) in the corresponding cell. Most type-S events radiate dilatational first motions parallel to the z-axis and compressional first motions parallel to the x-axis. This can also be seen from the primary data set of plus (Fig. 13b) and minus first-pulse polarities (Fig. 13c) of recorded acoustic emission wavelets. Pole diagrams include 803 plus (Fig. 13b) and 889 minus values (Fig. 13c), which are normalized to the total event number. Black indicates density values above 0.9; white values below 0.2. In the lower-hemisphere projection, horizontal plus poles (Fig. 13b) and vertical minus poles (Fig. 13c) are missing. This shows that rock material is shifted inside the cylinder in the vertical direction (z-axis) and outside in the horizontal direction (x-axis). In addition, from Fig. 13(a) the approximate orientation of the two average nodal planes is obtained from regions with accumulated zero polarity (Fig. 13a, dashed lines). This is similar to the determination of the composite fault plane and the auxiliary fault plane from the boundaries of dihedra (Angelier 1984). The first average nodal plane dips at 38° and has an azimuth (strike angle) of 180°. The second average plane is dipping 52° with a strike angle of 0° (x-axis). While the strike of the average AE fault plane solution is in good agreement with the observed fracture plane from tomogram sections (Figs 13a and 14a), the dip

Ag5w asymmetric

Figure 13. (a) Average fault plane solution of 212 single fault plane solutions of type-S microfracturing events detected during the asymmetric pre-fracture of core Ag5w. Percentage values indicate normalized positive and negative first motions in 400 accumulation cells. Density contours of plus (b) and minus (c) first-pulse polarity values of acoustic emission wavelets for the same events. Each data set is shown in conventional lower focal hemisphere (x–y) and unconventional side focal hemisphere (x–z) projections.

© 1998 RAS, GJI **135,** 1113–1130
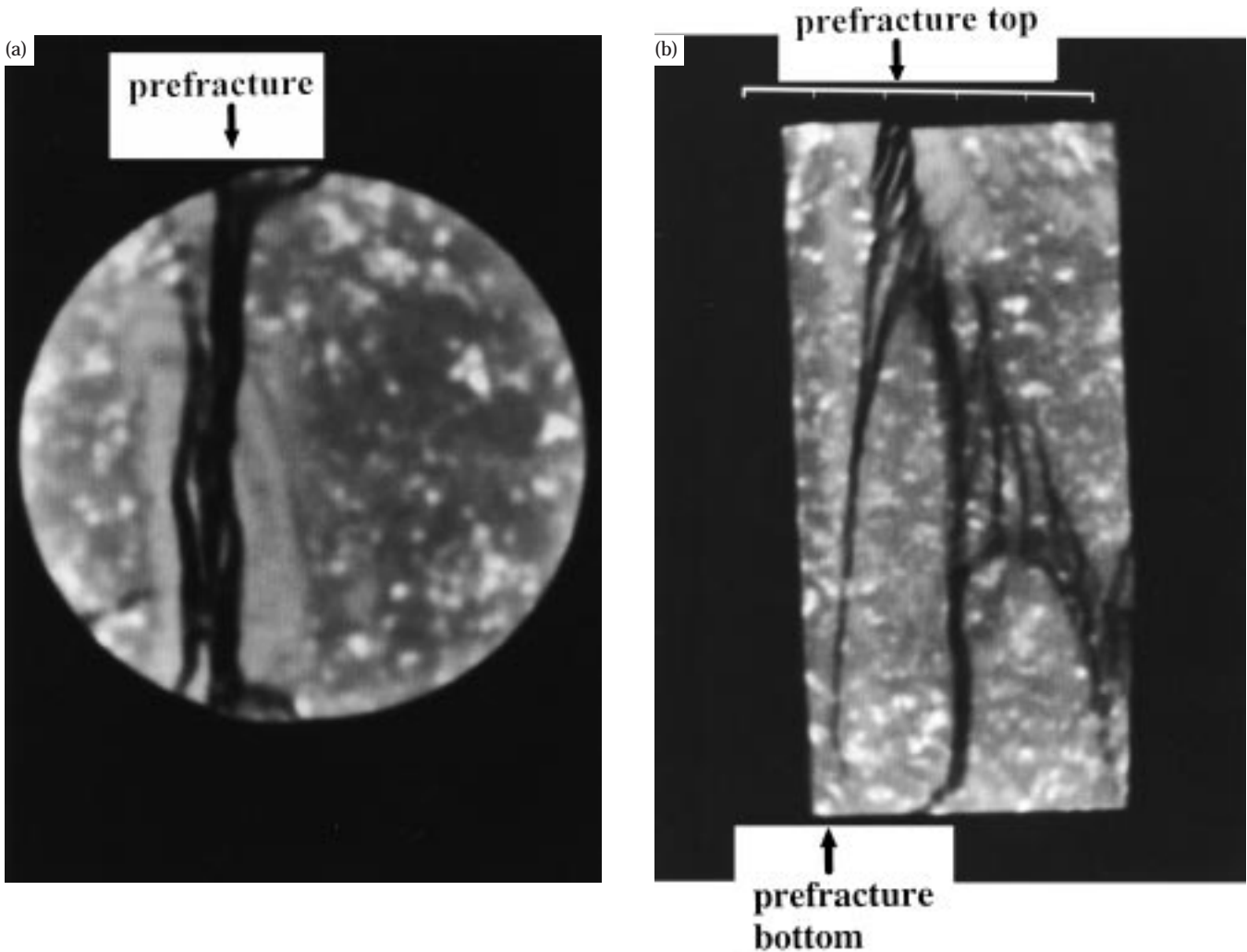
Figure 14. (a) Horizontal X-ray computer tomogram (x–y-plane) 5 mm below the asymmetrically loaded top surface of core Ag5w. Black indicates open fracture. Core diameter is 52 mm. (b) Vertical tomogram section (x, y = ±1 mm, z) of the same core. Top and bottom of the asymmetric failure are shown by arrows. Scale bar is 50 mm.

value differs (Figs 13a and 14b). One possible explanation for this is the change in orientation of the fracture plane from top to bottom of the core (Figs 5 a1 and 12), while the fault plane solution in Fig. 13 represents an average over all type-S events connected with the asymmetric shear rupture. A second explanation is that the asymmetric uniaxial compression test can produce a different movement along the shear rupture plane, as is known from shear ruptures in triaxial compression. A third explanation is that the uniaxial shear rupture has a tensile component due to the lack of confinement.

The average type-S event solutions of symmetric tests analogous to Fig. 13(a) show maximum values of dilatational and compressional pulses of ±20 per cent. The maximum density of dilatational pulses is also subparallel to the z-axis. Because of expected cone fractures, a more homogeneous distribution of dilatational and compressional pulses is obtained in vertical projections.

3.5 Fracture pattern from tomograms

The fracture pattern after deformation of the asymmetrically loaded core Ag5w is shown in Fig. 14. Fig. 14(a) shows a

horizontal tomogram (x–y-section) taken 5 mm below the core top surface (Fig. 2, x, y, z = 94 ± 1 mm). The asymmetric fracture (Fig. 14a, black) is located at the edge of the loaded (right) and unloaded (left) part of the granite cylinder. Fig. 14(b) shows a vertical tomogram (x–z-section) taken from a rock slice 2 mm in thickness from the central part of the same core (Fig. 2, x, y = ±1 mm, z) after final failure. The asymmetric fracture (Fig. 3d, t = 850 s) runs from the top (x = −10, y = 0, z = 100 mm) to the bottom of the core (Fig. 14b, pre-fracture arrows top and bottom). X-ray CT cannot resolve the bottom tip of the fracture, which is determined by conventional inspection of thin sections (x = −50, y = 0, z = 0 mm). The process of final failure of the core (Fig. 3d, t > 1800 s), which is excluded from discussion, is represented in Fig. 14(b) by a set of nearly vertical fractures in the central and right parts of the remaining core material.

Fig. 15 shows a 3-D view of fractures in the symmetrically loaded core Ag7w, reconstructed from 50 measured 2-D X-ray tomograms. The fracture network is extracted by subtracting the average signature of the rock matrix of the undeformed core. From spatial views, local small-scale changes of fracture orientation are observed, even though the overall macroscopic
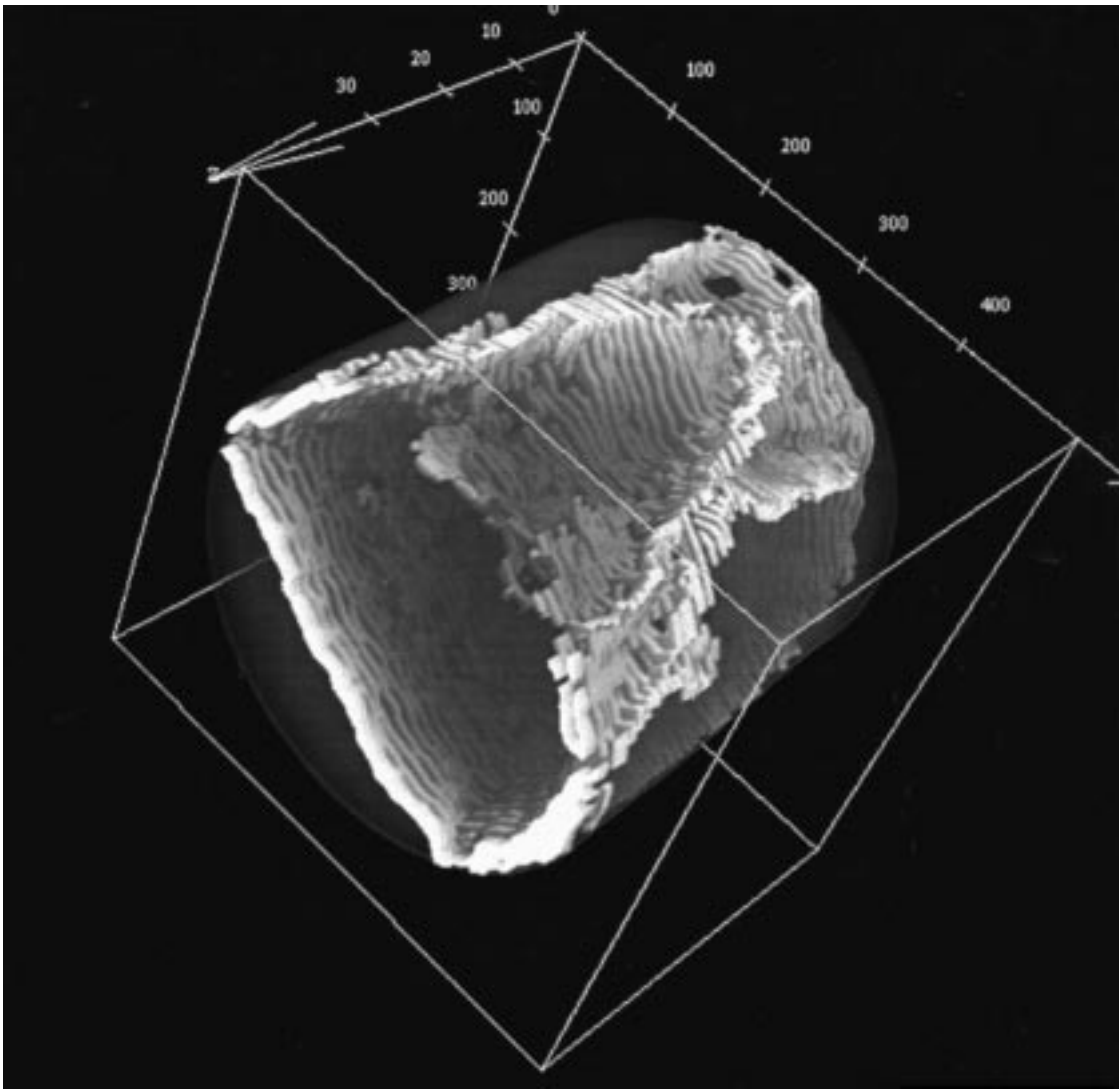
Figure 15. Reconstructed spatial view of fracture planes (white) from 2-D tomogram sections of core Ag7w after symmetric loading. Uniaxial compression direction was parallel to z-axis.

cone character of the fracture plane is preserved. This is another possible explanation for variable orientations of large type-S quakes despite their localization along a pre-defined shear plane.

4   DISCUSSION

The localization analysis of acoustic emissions in rock stressed to failure is a common tool for investigating fracture processes in geomaterials. Most studies deal with fracture propagation in rock cores under uniaxial compression with confinement (Lockner 1995), which is appropriate for simulating Earth's crustal stresses. The uniaxial tests described in this paper were carried out to test the sensitivity of selected AE parameters to changing stress boundary conditions. The evolution of hypocentre data (the correlation of event clusters in space and time) and emission wavelet parameters (amplitude and pulse energy) was investigated in different isostress volumes during the growth of a granite shear fracture.

From a physical point of view, our asymmetric tests represent a new approach in understanding the brittle failure of rock under controlled laboratory conditions with the path of the propagating rupture front known. While symmetric tests, either uniaxial or triaxial, carry the ambiguity of the final fault propagation path, the asymmetric test eliminates this degree of freedom. A different physical approach comes from recent precursory localization studies on rock material containing healed joints (Satoh et al. 1996). In both approaches the localization of the future emission concentrator is pre-determined; it is either a stress or a material heterogeneity. Furthermore, in the first case, the fracture initiation and fracture end are also known, which is not always the case in rock with naturally healed joints.

Hypocentre density distributions (Figs 4 and 5) and hypo-centre correlation data (Figs 6, 7 and 8) show that asymmetric tests with smaller isostress volumes (Fig. 1) produce both a greater number of located events and a more localized distri-bution of events compared to the symmetric case. The event

density is most sensitive to stress (for example, it doubles from symmetric to asymmetric loading), while the rock microstructure [e.g. average grain sizes 1.3 (Agr) and 1.7 mm (Agw)] is less important for the Aue granite specimens. Hypocentre density contours at different time sections of the experiment allow one to follow the process zone of the asymmetric fracture from the top to the bottom of the core (Fig. 5). The total time for this process observed in core Ag5w is 38 s.

The clustering of events is quantified by the fractal dimension D, obtained from standard correlation integral analysis C(r) (Hirata et al. 1987; Lei et al. 1992) and the modified current cluster analysis C(r = const.) versus time (Zang et al. 1996). The hypocentre correlation coefficient is 'directly proportional' to the event density and approximately reciprocally proportional to the fractal dimension (Figs 6, 7 and 8). The correlation analysis (Fig. 6), however, is less time-consuming and more reliable than D-values estimated from log–log plots of C(r) versus r (Figs 7a and 8a). Both parameters are studied for comparison with previous findings. The clustering of events in uniaxial compression (asymmetric or symmetric) is restricted to the post-failure region of rock, as was observed in triaxial compression tests (Lockner et al. 1992). In our uniaxial tests on Aue granite the fractal dimension dropped to 1.7 in symmetric and 1.2 in asymmetric failure (Table 1). Triaxial experiments on Inada granite led to minimum D-values of 2.2 (Lei et al. 1992) and triaxial experiments on Westerly granite to 1.7 (Lockner & Byerlee 1995). This shows that the localization of deformation in uniaxial asymmetric failure is greater than for all other loading scenarios. In any case, no anomaly is observed in granite specimens (Lei et al. 1992; Lockner & Byerlee 1995; this study). Prior to fault nucleation, a systematic decrease in D is only observed in Berea sandstone (Lockner & Byerlee 1995).

Independent of the material investigated, b-values from acoustic emission amplitude statistics indicate anomalies before the macroscopic mechanical response of rock (Main et al. 1989; Meredith et al. 1990; Lockner et al. 1991; Main et al. 1992). This is also true for wet specimens, where a double b-value anomaly is produced (Sammonds et al. 1992). The drop in b-value before failure of Aue granite is significant. It is 36 per cent for the symmetric and 42 per cent for the asymmetric test scenario. For comparison, the drop in b-value before dry and wet sandstone failure is up to 70 per cent. This is confirmed in triaxial experiments on Darley Dale sandstone (Main et al. 1993), triaxial tests on Gosford sandstone (Seto et al. 1996) and uniaxial tests on Flechtingen sandstone (Zang et al. 1996). While the b-value from amplitude–frequency distributions of AE seems to be a possible brittle failure precursor over a wide range of rock types, the D-value from AE hypocentre distributions shows an anomaly in some materials (e.g. Berea sandstone) and no anomaly in others (e.g. Aue, Inada and Westerly granite). No significant change is found between b-values calculated from average maximum amplitude, average focal amplitude (both determined from eight location sensors) and pulse energy equivalents determined from one broad-band sensor. First-pulse amplitudes, however, lead to a constant b-value throughout the experiments. It is not clear if this is an artefact due to the automatic first-motion picker, or if this result has some physical meaning.

Our simple polarity statistics do not verify that type-S events are from shear cracks, but we proved that tensile sources (wing cracks in a resin cylinder) generate positive polarities at most sensors (type-T events). Implosion sources (type-C events) are of minor importance in Aue granite experiments, but were verified in the early stage of sandstone compaction (Zang et al. 1996). Especially for few sensors and single-event analysis, this approach can be misleading, since the results will depend on the geometry of the experiment and the microcrack orientation. Using the cumulative polarity of event clusters and increasing the number of piezoceramic sensors from eight to 12, the results reported in Table 1 were confirmed in a suite of asymmetric tests with AE rate as the feedback signal. That is why we postulate that type-S events dominate 70 per cent of the microfracturing in uniaxial compression failure of Aue granite, independent of stress boundary conditions. This result is in disagreement with the observed switch in microfracturing mechanism from type-T to type-S approaching triaxial compressional failure of Oshima granite with a 1 mm grain size (Lei et al. 1992). It is in agreement with the finding of type-S events dominating in triaxial experiments on Inada granite with an average grain size of 5 mm (Lei et al. 1992) and uniaxial symmetric compression experiments on Charcoal granite with an average grain size of 2 mm (Shah & Labuz 1995). Lei et al. (1992) had 20 sensors, leading to a much better coverage of observation points on the focal sphere in their symmetric tests. In the asymmetric tests we used only eight sensors, but the orientation and propagation direction of fracture was predefined. The results obtained by moment tensor inversion (Shah & Labuz 1995) were also based on an array with eight sensors.

Large type-S emission events align along the future asymmetric fracture plane, but single nodal plane orientations can be poorly constrained (Fig. 12). Additionally, it is not clear that the events are true double couples, which is an a priori assumption for the fault plane solutions in Fig. 12. For example, Satoh et al. (1990) found that 50 per cent of events occurring under triaxial compression tests are type-S but are not compatible with the double-couple radiation pattern. This can explain why nodal planes of single fault plane solutions are 'randomly oriented' against the failure plane.

Average fault plane solutions of type-S events, irrespective of amplitude, are compared with the orientation of the macroscopic fracture plane from thin section and tomogram analysis (Figs 13a and 14). Whereas the fracture azimuth is well constrained by average fault plane solutions (Figs 13a and 14a), the fracture dip in tomograms (Fig. 14b, 70–80°) deviates from average nodal planes (Fig. 13a, 38 or 52°). We give three possible explanations for this. First, it may be caused by the change in fracture orientation due to effects from the core free surface. Second, the asymmetric uniaxial compression test assembly can induce shear failure with different displacement distributions on the rupture plane compared to triaxial tests with confinement. Third, the uniaxial asymmetric 'shear rupture' may have a tensile component due to zero confining pressure. Composite fault plane solutions in andesite also show a preferred orientation with respect to the healed joint (Satoh et al. 1996). Therefore, both average and composite fault plane solutions of type-S acoustic events can be helpful in determining the orientation of a macroscopic fracture plane in rock induced by either stress or material heterogeneities.

Future asymmetric experiments will operate with and without confining pressure and in a mode of AE rate control with one of 12 receivers as a servocontrol feedback signal in

order to slow down the rupture process. This set-up allows one to freeze in process zones of different sizes and to investigate the effect of strain rate on the size of the fracture process zone. Microstructural analyses of process-zone-related crack populations are under way.

5   CONCLUSIONS

New 'asymmetric' in combination with standard 'symmetric' uniaxial compression tests have allowed us to quantify the effect of stress anisotropy on the brittle failure of Aue granite. Using advanced acoustic emission techniques for mapping microfractures during rock failure and X-ray computer tomography for visualizing macroscopic failure planes in deformed cores, we draw the following conclusions.

(1) The failure in 'asymmetric' tests occurs in about half the time needed for producing 'symmetric cone failures' using a strain rate of $10^{-5} \, s^{-1}$. In the asymmetric test both a greater quantity (maximum event density doubles) and more localized distributions of acoustic emission hypocentres (correlation coefficient doubles) are observed.

(2) Possible failure precursors based on the correlation of event hypocentres in space and time are not observed in Aue granite. Prior to fault nucleation the negative slope of amplitude–frequency distributions (b-value) shows a significant anomaly before the macroscopic mechanical rock response. While the first statement seems dependent on, the second seems independent of the material investigated.

(3) No significant change between b-values calculated from average maximum amplitude and average focal amplitude corrected for geometric spreading, both obtained from eight location sensors, and acoustic emission energy obtained from one broad-band sensor is observed. Average first-pulse amplitudes from location sensors, however, show no anomaly prior to failure.

(4) Type-S acoustic emission events with equal ratios of plus and minus first motions dominate the uniaxial failure of Aue granite, irrespective of the stress boundary conditions. Additionally, the six largest (in terms of focal amplitude) type-S events align parallel to the later asymmetric fracture plane, but in no chronological order.

(5) Nodal planes from average fault plane solutions of microscopic emission events coincide in azimuthal direction (strike angle) with the overall orientation of the macroscopic fracture plane determined from tomograms and thin sections. This is not the case for the dip angle.

REFERENCES

Andresen, R., Zang, A., Hakim, S., Haidekker, M.A., Wagner, F.C., Banzer, D. & Dresen, G., 1997. Fracture pattern analysis of laboratory compressed rock cores by high resolution computed tomography (HRCT), Imaging, Science & Oncology, British J. Radiology, **70** (suppl), 131.

Angelier, J., 1984. Tectonic analysis of fault slip data sets, J. geophys. Res., **89**(B7), 5835–5848.

Dahm, T., 1996. Relative moment tensor inversion based on ray theory: theory and synthetic tests, Geophys. J. Int., **124**, 245–257.

Grassberger, P., 1983. Generalized dimensions of strange attractors, Phys. Lett., **97**, 227–230.

Grosse, C.U., Reinhardt, H.W. & Dahm, T., 1997. Localization and classification of fracture types in concrete with quantitative acoustic emission measurement techniques, J. Non-Destructive Testing Evaluation, **30**, 223–230.

Hanks, T.C., 1992. Small earthquakes, tectonic forces, Science, **256**, 1430–1432.

Hirata, T., Satoh, T. & Ito, K., 1987. Fractal structure of spatial distribution of microfracturing in rock, Geophys. J. R. astr. Soc., **90**, 369–374.

Hori, M. & Maro, E., 1995. Micromechanical analysis of anomalous behavior of b-value of rock, in Mechanics of Jointed and Faulted Rock, pp. 85–90, ed. Rossmanith, H.-P., Balkema, Rotterdam.

Jackson, J.A. & McKenzie, D.P., 1988. The relationship between plate motions and seismic moment tensors and the rates of active deformation in the Mediterranean and Middle East, Geophys J., **93**, 45–73.

Kusunose, K., 1995. Fracture mechanics of rocks, J. Phys. Earth, **43**, 479–504.

Lei, X., Nishizawa, O., Kusunose, K. & Satoh, T., 1992. Fractal structure of the hypocenter distributions and focal mechanism solutions of acoustic emission in two granites of different grain sizes, J. Phys. Earth, **40**, 617–634.

Lockner, D. & Byerlee, J.D., 1993. How geometric constraints contribute to the weakness of mature faults, Nature, **363**, 250–252.

Lockner, D.A., 1993. The role of acoustic emission in the study of rock fracture, Int. J. Rock Mech. Mining Sci. Geomech. Abstr., **30**, 883–899.

Lockner, D.A., 1995. Rock failure, in Rock Physics and Phase Relations, A Handbook of Physical Constants, AGU Reference Shelf, Vol. 3, pp. 127–147.

Lockner, D.A., 1996. Brittle fracture as an analog to earthquakes: can acoustic emission be used to develop a viable prediction strategy, J. acous. Emission, **14**, S88–S101.

Lockner, D.A. & Byerlee, J.D., 1995. Precursory AE patterns leading to rock fracture, in Proc. 5th Conf. on Acoustic Emission/Microseismic Activity in Geologic Structures and Materials, pp. 45–58, ed. Hardy, H.R., Trans-Tech, Clausthal-Zellerfeld, Germany.

Lockner, D.A., Byerlee, J.D., Kuksenko, V., Ponomarev, A. & Sidorin, A., 1991. Quasi-static fault growth and shear fracture energy in granite, Nature, **350**, 39–42.

Lockner, D.A., Byerlee, J.D., Kuksenko, V., Ponomarev, A. & Sidorin, A., 1992. Observations of quasistatic fault growth from acoustic emissions, in Fault Mechanics & Transport Properties of Rocks, pp. 3–31, eds Evans, B. & Wong, T.-F., Academic Press, London.

Main, I.G., 1992. Damage mechanics with long-range interactions: correlation between the seismic b-value and the fractal two-point correlation dimension, Geophys. J. Int., **111**, 531–541.

Main, I.G., Meredith, P.G. & Jones, C., 1989. A reinterpretation of the precursory seismic b-value anomaly from fracture mechanics, Geophys. J., **96**, 131–138.

Main, I.G., Meredith, P.G. & Sammonds, P.R., 1992. Temporal variations in seismic event rate and b-values from stress corrosion constitutive laws, Tectonophysics, **211**, 233–246.

Main, I., Sammonds, P.R. & Meredith, P.G., 1993. Application of a modified Griffith criterion to the evolution of fractal damage during compressional rock failure, Geophys. J. Int., **115**, 367–380.

Manthei, G. & Eisenblatter, J., 1993. Mikroakustische Messungen im Salzgestein, Kali und Steinsalz, **11**, Heft 3/4, 94–101.

Meglis, L., Chow, T.M. & Young, R.P., 1995. Progressive microcrack development in tests on Lac du Bonnet Granite-I. Acoustic emission source location and velocity measurements, Int. J. Rock Mech. Min. Sci. Geomech. Abstr., **32**, 741–750.

Meredith, P.G., Main, J.G. & Jones, C., 1990. Temporal variations in seismicity during quasi-static and dynamic rock failure, Tectonophysics, **175**, 249–268.

Mogi, K., 1962. Magnitude-frequency relation for elastic shocks accompanying fractures of various materials and some related problems in earthquakes, 2, Bull. Earthq. Res. Inst., **40**, 831–853.

MTS Systems Corporation, 1996. Rock and Concrete Mechanics Testing Systems—Technical Description, Eden Prairie, MN.

Ohtsu, M., 1996. Generation of acoustic emission waves and moment tensor analysis, J. acous. Emission, **14**, S103.

Paterson, M.S., 1978. Experimental Rock Deformation—the Brittle Field, Springer-Verlag, Berlin.

Peng, S. & Johnson, A.M., 1972. Crack growth and faulting in cylindrical specimens of Chelmsford granite, Int. J. Rock Mech. Min. Sci., **9**, 37–86.

Press, W.H., Flamery, B.P., Tenkolsky, S. & Vetterling, W.T., 1987. Numerical Recipes, Cambridge University Press, Cambridge.

Rummel, F., 1982. Fracture and flow of rocks and minerals, in Landolt-Bornstein, Physical Properties of Rocks, Vol. 1b, pp. 141–238, ed. Angenheister, G., Springer, Berlin.

Sammonds, P.R., Meredith, P.G. & Main, I.G., 1992. Role of pore fluids in the generation of seismic precursors to shear fracture, Nature, **359**, 228–230.

Satoh, T., Nishizawa, O. & Kusunose, K., 1990. Fault development in Oshima Granite under triaxial compression inferred from hypocenter distribution and focal mechanism of acoustic emission, Tohoku geophys. J., **33**, 241–250.

Satoh, T., Shivakumar, K., Nishizawa, O. & Kusunose, K., 1996. Precursory localization and development of microfractures along the ultimate fracture plane in amphibolite under triaxial creep, Geophys. Res. Let., **23**, 865–868.

Scholz, C.H., 1968. The frequency-magnitude relation of micro-fracturing in rock and its relation to earthquakes, Bull. seism. Soc. Am., **58**, 399–415.

Seto, M., Nag, D.K. & Vutukuri, V.S., 1996. Acoustic emission behavior of dry and saturated sandstone under triaxial compressive stress conditions, 5th Int. Symp. Mine Planning and Equipment Selection, pp. 269–274, Sao Paulo, Brazil.

Shah, K.R. & Labuz, J.F., 1995. Damage mechanisms in stressed rock from acoustic emission, J. geophys. Res., **100**, 15 527–15 539.

Zang, A., Wagner, F.C. & Dresen, G., 1996. Acoustic emission, microstructure, and damage model of dry and wet sandstone stressed to failure, J. geophys. Res., **101**, 17 507–17 521.

APPENDIX A: CORE STRESS CALCULATED BY FINITE ELEMENTS

In order to interpret crack growth with acoustic emission hypocentre distributions, a precise knowledge of the stress field inside the deformed granite cylinders is necessary. For this purpose, a 3-D finite element calculation is carried out using the software package MARC, with integrated pre- and post-processor MENTAT (MARC Software Deutschland GmbH,

Aschheim). The granite cylinder, measuring 100 mm in length and 52 mm in diameter, is modelled as a homogeneous elastic isotropic body with a Young's modulus of 63 GPa and a Poisson's ratio of 0.16. The first elastic constant is determined from the linear part of the stress–strain curve, the latter from ultrasonic P- and S-wave pulse transmission measurements. For boundary conditions we prescribed displacements at the core top surface (area 1691 mm2 for asymmetric and 2124 mm2 for symmetric loading). The value of vertical displacement ($u_z = -0.288$ mm) was taken from the MTS data file for the critical displacement value shortly before the pre-fracture of sample Ag5w took place. The bottom surface of the cylinder was fixed by boundary conditions, where horizontal displacements were zero ($u_x = u_y = 0$), simulating clamped end caps between rock and compression steel plates.
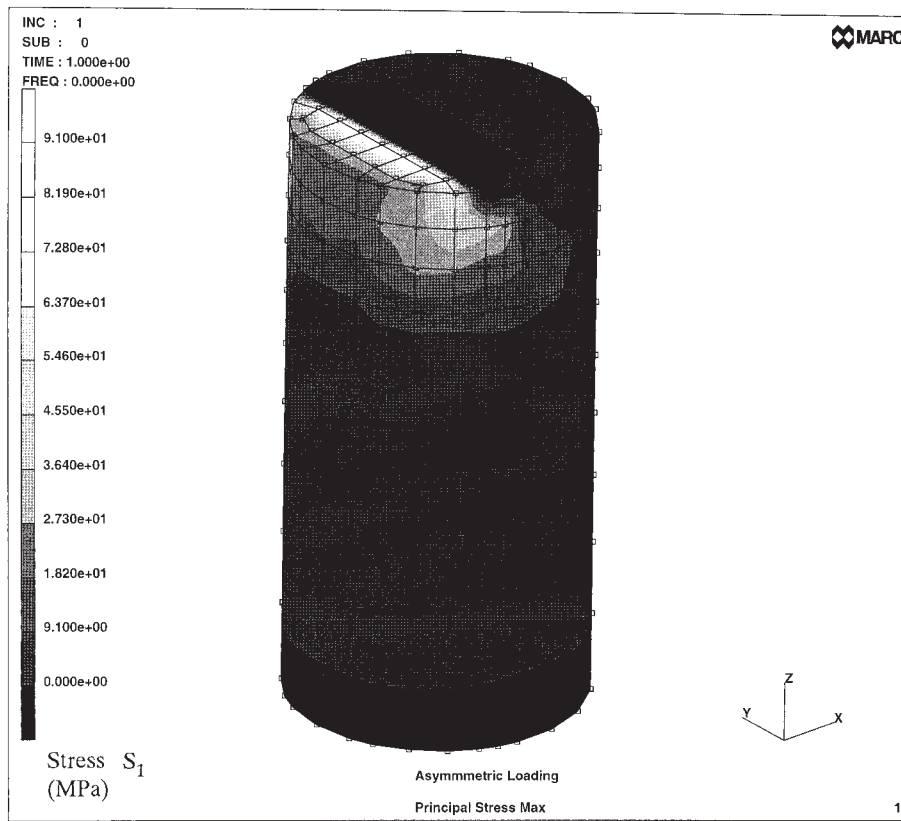
In Table A1 extreme values of calculated stress components are listed for the asymmetric case at a stage shortly before the experimental granite sample fails. Tension is positive. The vertical displacement $u_z = -0.288$ mm taken as input was obtained from the laboratory data record of core Ag5w. Maximum tensile stress can be inferred from the maximum principal stress ($S_1 = 91$ MPa). Maximum Cartesian shear stress is –151 MPa and occurs in the x–z-plane (Table A1, S_{zx}). In order to decide where tensile failure and where shear failure are expected, the spatial distributions of the stress components S_1 and S_{zx} inside the core are plotted in Fig. A1. Fig. A1(a) shows modelled maximum principal stress contours restricted to tensile values ($0 < S_1 < 91$ MPa). Black areas indicate compressive stress ($S_1 < 0$). White indicates the region with highest tensile stress, which is located on the top surface of the core next to the asymmetric loading plate. Note that considerable tensile stresses ($S_1 > 20$ MPa) also occur 20–30 mm below the top surface inside the unloaded part of the rock cylinder. Fig. A1(b) quantifies the maximum Cartesian shear stress ($-151 < S_{zx} < 67$ MPa). The maximum value is located sub-parallel to the y-axis shifted about 5 mm from the edge of the asymmetric loading plate. Also, in the load-bearing part of the core, shear stresses develop due to the bending moment at the top surface. These shear stresses are of a lower magnitude than and of opposite sign ($S_{zx} < 67$ MPa) to those in the unloaded part of the specimen. From this analysis, rock failure is expected to initiate in tensile mode at the edge of the loading

Table A1. Stress magnitudes inside a granite core during asymmetric loading calculated from measured critical vertical displacement at failure ($u_z = -0.288$ mm). Tension is positive.
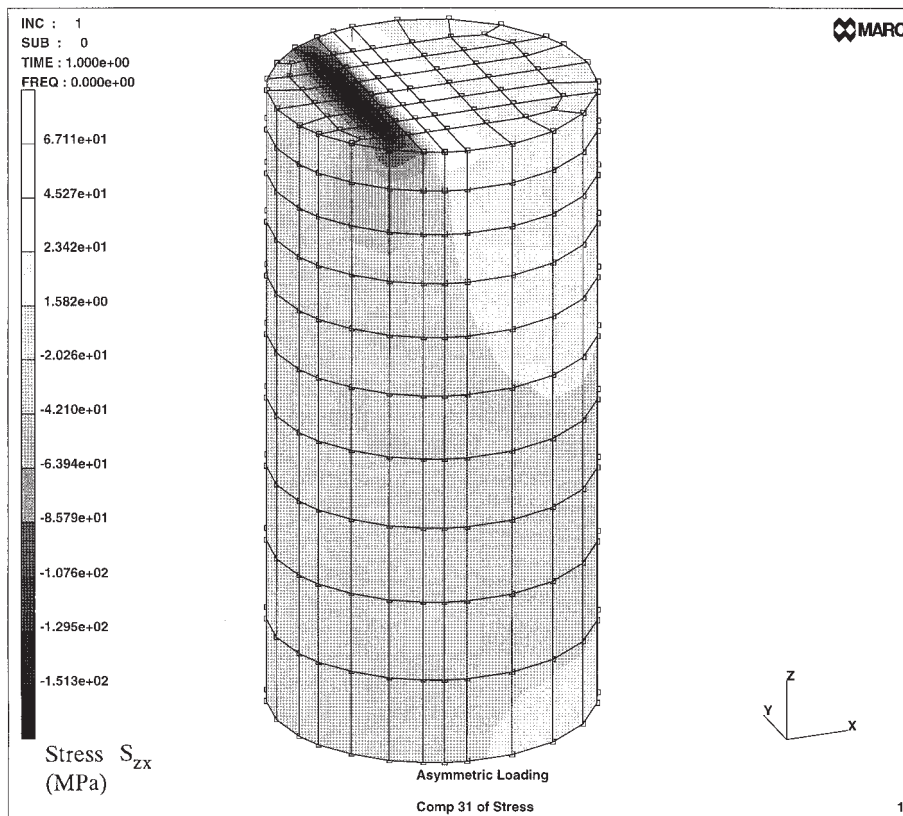
Stress (MPa)	Min.	Max.	
S_{xx}	−211	35	normal
S_{yy}	−60	27	stress
S_{zz}	−438	17	
S_{xy}	−25	25	shear
S_{yz}	−27	27	stress
S_{zx}	−151	67	
S_1	−38	91	principal
S_2	−156	19	stress*
S_3	−562	9	

* $S_1 > S_2 > S_3$

Figure A1. (a) Principal maximum stress restricted to tensile values $(0 < S_1 < 91 \text{ MPa})$ and (b) maximum Cartesian shear stress $(-151 < S_{zx} < 67 \text{ MPa})$ inside the asymmetrically loaded granite core calculated by a 3-D finite element model at a stage shortly before the experimental granite sample failed.

© 1998 RAS, GJI **135,** 1113–1130

plate and to propagate with a dominating shear component into the unloaded part of the asymmetrically loaded cylinder.

The calculated maximum tensile stress at failure is considerably higher than tensile strength values of granite from Brazilian or Hydrofrac tests. For example, for Falkenberg granite a maximum tensile strength value of 20 MPa is reported (Rummel 1982). The calculated maximum shear stress at failure ($S_{XZ} = -151$ MPa) is comparable to the value of maximum shear strength from Coulomb theory. With maximum principal stresses (Table A1, $S_1 = 91$ MPa, $S_3 = -560$ MPa) and the observed fracture plane orientation with respect to the compression direction (Fig. 14b, $10°-15°$) the Mohr–Coulomb criterion leads to granite shear strength values between 111 and 163 MPa.